DEVELOPMENT OF GRAPHENE/SILICON CARBIDE BASED QUADRANT PHOTODETECTOR DEVICE

A Thesis Submitted to
The Graduate School of
İzmir Institute of Technology
in Partial Fulltime of the Requirements for the Degree of

MASTER OF SCIENCE

in Physics

by
Ahmet Yusuf REYHAN

July 2025

İZMİR

We approve the thesis of **Ahmet Yusuf REYHAN**

Examining committee members:

Prof. Dr. Cem ÇELEBİ
Department of Physics, İzmir Institute of Technology

Assoc. Prof. Dr. Günnur GÜLER
Department of Physics, İzmir Institute of Technology

Assoc. Prof. Dr. Gökhan UTLU
Department of Physics, Ege University

18 July 2025

Prof. Dr. Cem ÇELEBİ
Supervisor, Department of Physics,
İzmir Institute of Technology

Asst. Prof. Dr. Özhan ÜNVERDİ
Co-Supervisor, Department of
Electrical and Electronic Engineer,
Yasar University

Prof. Dr. Alev Devrim GÜÇLÜ
Head of the Department of Physics

Prof. Dr. Mehtap EANES
Dean of the Graduate School

ACKNOWLEDGMENTS

I would like to express my deepest gratitude to my supervisor Prof. Dr. Cem ÇELEBİ, who has been more than an academic advisor to me throughout my journey. Coming from an electronics engineering background, I was able to fulfil my aspirations in both electronics and experimental physics through my work in Quantum Device Laboratory. Under his guidance I was able to gain experience in materials fabrication, operation and troubleshooting of complex equipment such as high vacuum laboratory systems. He taught me how to work – how to approach problems both as an engineer and as a researcher. His mentorship not only shaped my academic path but also how I carry myself in life and work. For all of this, I will remain profoundly grateful throughout my life.

I would like to thank my committee members of my thesis Assoc. Prof. Dr. Gökhan UTLU and Assoc. Prof. Dr. Günnur GÜLER for their support and guidance.

I will be forever grateful for having the privilege of working in the friendly environment of Quantum Device Laboratory and express my gratitude towards my friends Atilla Mert DÜLCEL, Melike GÖZEK and Tuana BARANDIR for their support and collaboration.

In addition, I would like to thank Dr. Özhan ÜNVERDİ for introducing me to this path and teaching me physics in my first undergraduate years, I am also thankful to Prof. Dr. Alev Devrim GÜÇLÜ for his efforts in teaching me quantum mechanics.

This work is supported by Yaşar University Project Evaluation Commission (PEC) under the scope of the Project No. BAP143.

Lastly, I want to thank myself for never giving up against all odds and fulfilling this dream of 7 years through hard work.

ABSTRACT

DEVELOPMENT OF GRAPHENE/SILICON CARBIDE BASED QUADRANT PHOTODETECTOR

In this thesis work, a self-biased, Schottky-junction quadrant photodetector device operating in the ultraviolet region, based on a Graphene/Silicone Carbide device architecture was designed and characterized. The aim of the study is to evaluate the compatibility of p-type graphene synthesized by chemical vapour deposition with the quadrant photodetector architecture and to experimentally investigate its light position sensing capability. The electrodes and structure of the quadrant device were formed on a silicon carbide substrate, which constitutes the n-type junction, using thermal evaporation method. The bilayer p-type graphene was verified through Raman spectroscopy. Dark current-voltage characteristics of the device were measured. The device's responsivity to ultraviolet light in 250 – 300 nanometer wavelength range was measured. Finally, the positioning accuracy was determined by scanning within the active region of the sensor in a defined search grid. This study provides foundational reference for future development of quadrant photodetectors based on Graphene/Silicon Carbide architecture.

ÖZET

GRAFEN/SİLİSYUM KARBÜR TABANLI QUADRANT FOTODEDEKTÖR AYGIT GELİŞTİRİLMESİ

Bu tez çalışmasında, Kimyasal Buhar Biriktirme yöntemi ile üretilen p-tipi grafen ve n-tipi Silisyum Bu tez çalışmasında Grafen/Silisyum Karbür aygıt mimarisine sahip kendinden beslemeli, Schottky eklemli ve ultraviyole bölgede çalışacak kadran fotodedektör aygıt tasarlanmış ve karakterize edilmiştir. Çalışmanın amacı kapsamında kimyasal buhar biriktirme metodu ile sentez edilmiş p-tipi çift katmanlı grafen malzemesinin kadran fotodedektör mimarisine uyumluluğunu değerlendirilmiş ve ışık pozisyonunu algılama kapasitesini deneysel metodlar ile incelenmiştir. Aygıtın n-tipi eklemini oluşturan silisyum karbür alttaşın üzerinde termal buharlaştırma metodu ile kadran aygıtın elektrotları ve yapısı oluşturulmuştur. Çift katmanlı p-tipi grafen bu yapının üzerine transfer edilerek p-i-n eklemlerine sahip kendinden beslemeli aygıt yapısı tamamlanmıştır. Büyütülmüş çift katmanlı grafenin varlığı Raman spektroskobisi metodu ile doğrulanmıştır. Aygıtın karanlık koşullarda akım-gerilim özellikleri ölçülerek, karanlık akım, Schottky bariyer yüksekliği ve idealite faktörleri hesaplanmıştır. Cihazın 250 – 300 nanometre dalga boyundaki ultraviyole ışınına karşı tepkiselliği ölçülmüştür. Son olarak pozisyonlama hassasiyeti sensörün aktif bölgesinde seçilen bir aramada tarama yaparak belirlenmiştir. Bu çalışma gelecekte geliştirilebilecek Grafen/Silisyum Karbür mimarisine sahip kadran fotodedektörler için bir giriş niteliği taşımaktadır.

to my grandmother

TABLE OF CONTENTS

LIST OF FIGURES

Figure **Page**

LIST OF TABLES

LIST OF SYMBOLS

C	Carbon
σ	Sigma
q	Elementary charge
p	Concentration of holes
Φ_M	Work function of metal
Φ_S	Work function of the semiconductor
R_s	Series resistance
η	Ideality factor
Φ_B	Barrier height
χ	Electron affinity
I_{SM}	Semiconductor-to-metal current density
A*	Richardson constant
T	Temperature
k_b	Boltzmann constant
k	Linear parameter
I_{MS}	Metal-to-semiconductor current density
Cu	Copper
H_2	Hydrogen
Ar	Argon
I_G	G Intensity of graphene on Raman
I_{2D}	2D Intensity of graphene on Raman
$FeCl_3$	Iron (III) chloride
HCl	Hydrochloric acid
HF	Hydrofluoric acid
SiO_2	Silicon oxide
Ni	Nickel
Cr	Chromium

Al	Aluminium
Au	Gold
I_0	Saturation currents
I_d	Dark currents
A	Junction area
R	Spectral response
P (λ)	Incident light power
D*	Specific detectivity
t_r	Rise time
t_f	Fall time

LIST OF ABBREVIATIONS

2D	Two dimensional
Gr	Graphene
SiC	Silicon Carbide
e-h	Electron-hole pairs
Gr/4H-SiC	Graphene/4H Silicone Carbide
UV	Ultraviolet
M/S	Metal/Semiconductor
CVD	Chemical vapor deposition
PR	Photoresist
DI	Deionized water
IPA	Isopropyl alcohol
PCB	Printed circuit board
LED	Light emitting diode
TE	Thermionic Emission
NEP	Noise equivalent power
SBH	Schottky Barrier Height
QDL	Quantum Device Laboratory
QPD	Quadrant Photodetector Device

CHAPTER 1

INTRODUCTION

1.1. Graphene

Graphene is the two-dimensional (2D) allotrope of carbon which is composed of a honeycomb structure lattice and it has attracted interest over the years in various research due to its optical and electronic properties.[1]

Before becoming an experimental reality, Geim et al. provides insight into the history and states that it was Landau and Peierls who claimed that two dimensional crystals could not remain thermodynamically stable.[2] It was widely believed that 2D materials would only exist as a part of a larger three-dimensional (3D) structure.[2,3,4] However, in 2004 Geim and Novoselov have successfully managed to isolate graphene from graphite by mechanical exfoliation and hence proved the existence of standing two-dimensional crystals.[5]

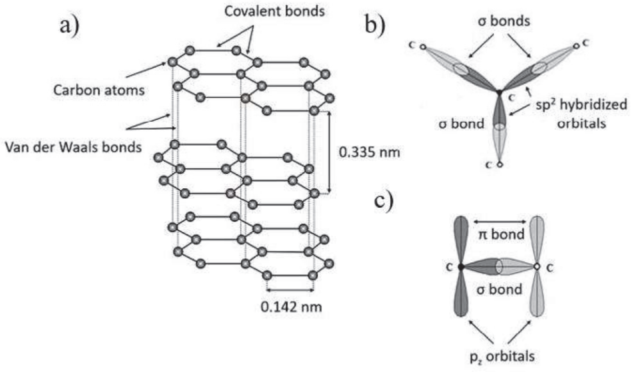

Figure 1.1. Graphene structure illustrated. a) Graphite structure composed of graphene layers held together by van der Waals. b) In-plane and c) out of plane bonds (image taken from reference 6).

Figure 1.1 a) shows the two-dimensional honeycomb lattice structure.[6] Carbon with 4 valence electrons forms covalent bonds with the 3 neighbouring carbon atoms.[6] Electrons are arranged in $1s^2$, $2s^2$, $2p^2$ orbitals. The s, p_x, p_y orbitals form the sp^2 hybridization which lies in the plane at 120° to each other forming strong σ (sigma) bonds with 3 neighbouring carbon atoms.[6] The remaining p_z orbitals form weak π (pi) bonds perpendicular to the plane with the neighbouring atoms. Figure 1.1 b) and c) show the σ-bond and π-bond respectively, mechanical properties of graphene such as robustness and elasticity are attributed to σ-bonds while formation of π-bonds results in exceptional electrical conduction properties.[6] Monolayer graphene is 0.335 nm thick while the distance between the carbon atoms is 0.142 nm.

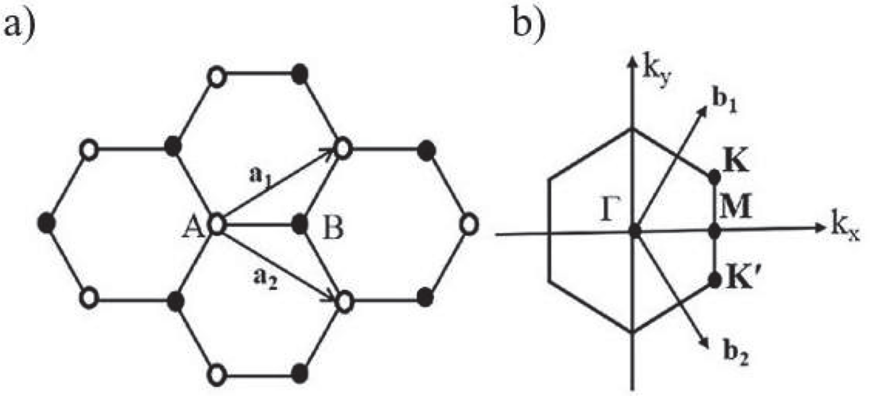

Figure 1.2. Graphene lattice schematics. a) Honeycomb structure in real space showing sublattices A and B. b) First Brillouin zone highlighting the high-symmetry points (image taken from reference 7).

As shown in Figure 1.2 a) there are two carbon atoms per unit cell in the hexagonal structure, these atoms are named as A and B, the real space lattice vectors are given by:[7]

$$\overrightarrow{a_1} = a\left(\frac{3}{2}, \frac{\sqrt{3}}{2}\right), \overrightarrow{a_2} = a\left(\frac{1}{2}, \frac{-\sqrt{3}}{2}\right) \quad (1.1)$$

Where term a denotes the lattice constant of 0.246 nm, the corresponding first Brillouin zone of the reciprocal lattice is shown in Figure 1.2. b) the center point is denoted as Γ, the inequivalent corners are K and K' finally the midpoint of each edge is defined as M.[7]

In equation (1.2) b_1 and b_2 define the first Brillouin zone of graphene in reciprocal space.[7]

$$\overrightarrow{b_1} = \frac{2\pi}{a}\left(\frac{1}{2},\frac{\sqrt{3}}{2}\right),\ \overrightarrow{b_2} = \frac{2\pi}{a}\left(\frac{1}{2},\frac{-\sqrt{3}}{2}\right) \quad (1.2)$$

Momentum space positions of the Dirac points (K and K') are defined in equation (1.3).[7]

$$\vec{K} = \frac{2\pi}{3a}\left(1,\frac{1}{\sqrt{3}}\right),\ \overrightarrow{K'} = \frac{2\pi}{3a}\left(1,\frac{1}{\sqrt{3}}\right) \quad (1.3)$$

Graphene is a zero-bandgap semiconductor, in other words the conduction and valence bands come in contact at six distinct points in the Brillouin zone, as shown in Figure 1.3.[7]

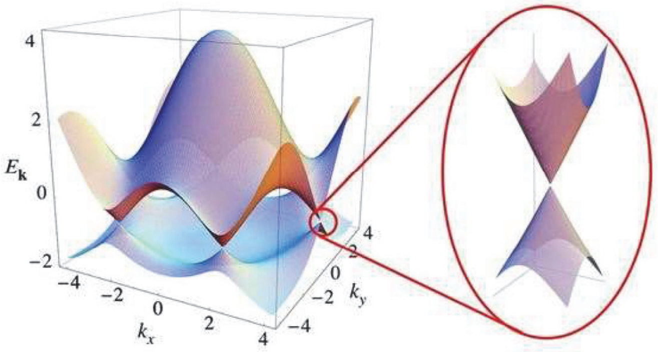

Figure 1.3. Electronic band structure of graphene. The conduction and valence bands meet at the Dirac points, inset shows the linear dispersion near the cone (image taken from reference 7).

In addition, the Fermi level is at the mid-point of these bands for intrinsic graphene .[8] The energy dispersion near the Dirac points can be expressed by the linear equation (1.4).[9]

$$E(k)^{+}_{-} = {}^{+}_{-}\hbar\, v_f|k| = {}^{+}_{-}\hbar\, v_f\sqrt{k_x^2 + k_y^2} \quad (1.4)$$

Where $\hbar$ denotes the reduced Planck constant, k is the wave vector and V_f is the fermi velocity. Due to linear distribution the charge carriers behave as relativistic and massless particles.[1]

1.2. Basics of Schottky Junction

Metal-semiconductor (M/S) junctions form one of the most fundamental structures in device physics. The concept was first established around 1960, it's defined by the formation of a potential barrier at the interface which defines its electrical characteristics, barrier properties are governed by the fermi level of the semiconducting material and work function of the metal.[10] By this relation two types of devices can be created namely Ohmic and Schottky. Conduction of current in Ohmic devices show linear behaviour which means such devices admit the flow of current while forward and reverse biased. Meanwhile due to the existence of a potential barrier with Schottky junction devices it is only possible for current to pass through one direction.[11] Table 1.1 show the relation between the work function of metal and semiconductor and the resulting type of contact.

Table 1.1. Type of contact in relation with the work functions of metal and semiconductor.

Work Function	**n-type semiconductor**	**p-type semiconductor**
$\Phi_M < \Phi_S$	Ohmic	Schottky
$\Phi_M > \Phi_S$	Schottky	Ohmic

Each metal is characterized by a specific work function Φ_M, when it contacts a semiconductor with electron affinity (Φ_S) the difference between these terms gives rise to the Schottky barrier.[12] Schottky diodes based on metal/semiconductor (M/S) junctions are typically described by key parameters such as the series resistance (R_s), the ideality factor (ɳ), and the barrier height (Φ_B). To analyse their current transport, the thermionic emission (TE) model is used, it accounts for the temperature dependence of the Schottky diode characteristics and enables extraction of these physical parameters.[13] To analyse their current transport, the thermionic emission (TE) model is used, it accounts for the temperature dependence of the Schottky diode characteristics and enables extraction of these physical parameters.[13]

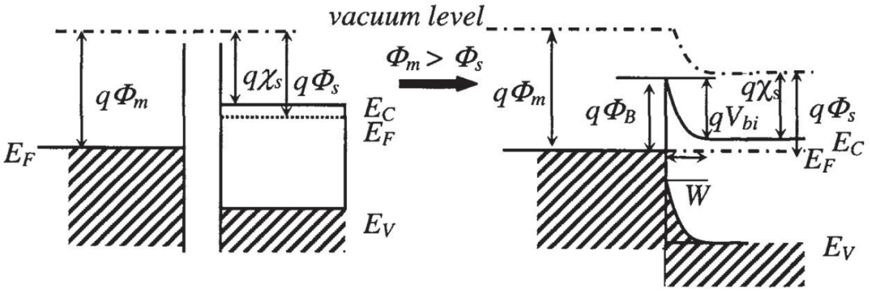

Figure 1.4. Energy band diagram of a metal-semiconductor (n-type) junction. On the left relative position of the metal work function and the semiconductor electron affinity is shown. On the right band bending and formation of the depletion region is given, Schottky barrier height is $q\Phi_B$.[14]

Figure 1.4 shows the energy band diagrams of metal-semiconductor contacts and the alignment after contact at thermal equilibrium. The barrier height relation is given in (1.5).[14] Applying forward or reverse bias causes the bands of the depletion region bend.

$$q\Phi_B = q(\Phi_M - \chi) \qquad (1.5)$$

When a forward or reverse bias is applied, the electric field across the depletion region is modified, which shifts the potential profile and causes the band to bend. In forward bias, the barrier is lowered, allowing the carriers to cross more easily while in reverse bias the barrier height effectively increases and restricts the current flow.

The current density from semiconductor to metal I_{SM} can be expressed as (1.6):[15]

$$I_{SM} = A^{*}T^{2}\left(\frac{-q\Phi_B}{k_BT}\right)\exp\left(\frac{qV}{k_BT}\right) \qquad (1.6)$$

Here (A^*) is the Richardson constant, (T) temperature, (k_B) Boltzmann constant. The total current density flowing from the metal into the semiconductor I_{MS} is shown in (1.7), its reduced form is given in (1.8):[15]

$$I_{MS} = A^{*}T^{2}exp\left(\frac{-q\Phi_B}{k_BT}\right)\left[\exp\left(\frac{qV}{\eta k_BT}\right) - 1\right] \quad (1.7)$$

$$I_{MS} = A^{*}T^{2}exp\left(\frac{-q\Phi_B}{k_BT}\right) \quad (1.8)$$

1.3. Gr/4H-SiC UV Photodetectors

Gr/4H-SiC photodetector devices combine graphene electrode with a wide-bandgap semiconductor SiC. Graphene serves as a transparent electrode that has up to 90% transmittance for the UV spectrum between 200 – 400 nm.[16] UV photons reach the substrate with minimal loss. Graphene also has high carrier mobility and conductivity.[17]

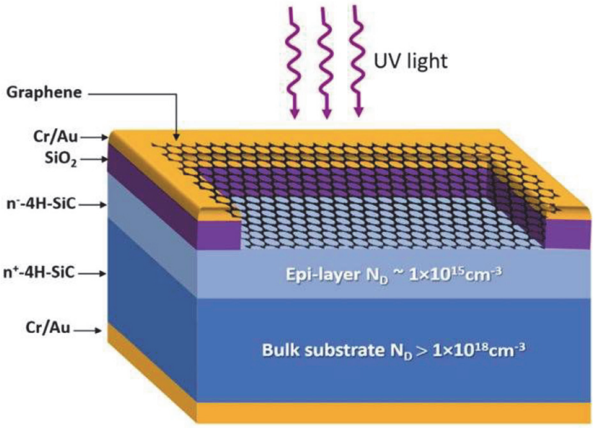

Figure 1.5. Schematic of Graphene/Silicone Carbide UV Photodetector device (taken from reference 18).

Ala et al. have fabricated a self-powered UV photodetector with p-i-n structure using bilayer graphene as a p-type electrode, the 4-H SiC substrate is composed of three layers.[18] Si-face of the substrate (n^- epilayer) has doping concentration of N_D ~ 1 x 10^{15} cm^{-3} with 3 μm thickness followed by n^+ epilayer with N_D ~ 1 x 10^{18} cm^{-3}. Finally, towards the C-face the substrate has a 350 μm thick bulk layer with N_D ~ 1 x 10^{19} cm^{-3}. This structure generates built-in electrical field. The schematic structure of the device is given in Figure 1.5.[18]

Device operation relies on the strong built-in electric field at the n^-/n^+ junction. Under UV illumination photons generate e-h pairs within the SiC, which are then efficiently separated by this field. Holes drift towards graphene and electrons drift towards the bulk side. Due to the abundance of holes in the epilayer side and the Schottky barriers carriers cannot escape and generation of significant photocurrent is prevented. Instead, this separation can be measured as a voltage and therefore the need to use transimpedance amplifier circuitry is eliminated.[18]

The single cell Gr/4H-SiC UV photodetector exhibited excellent performance with a low dark current of 0.58 nA also high spectral responsivity of 0.75 V/W was recorded[18].

Using the same substrate a quadrant structure was designed in this study, further experimental details and results are given at Chapter 2 and Chapter 3.

1.4. Nickel Oxide as an Electrical and Optical Isolator

To create quadrant structure on the Gr/4H-SiC photodetector device an optical isolator in the UV region needed to be found and a method to electrically isolate the p-type Gr junction of the fabricated device needed to be created.

Nickel oxide (NiO) is a wide bandgap semiconductor material that has a band gap close to 3.8 eV value, which makes it mostly transparent in the visible wavelengths but highly absorbent in the UV region[19]. Guziewicz et al. report the transmittance spectra of 300 nm NiO films deposited at different temperatures and oxygen amounts, it is proven that NiO has low transmittance in the UV region validating it as a suitable candidate to be used to separate graphene electrode.

1.5. Quadrant Photodetectors – Principles and Applications

Quadrant photodetectors (QPDs) consist of four photodiode elements arranged in one structure. Each element reacts to the incident light and generates photocurrent response. Comparing the intensity of the incident light falling on these channels the position of the spot can be determined with high accuracy. Position sensitive devices or QPDs are widely used for accurate position sensing and tracking both in the fields of military and civil applications.[20,21,22,23]

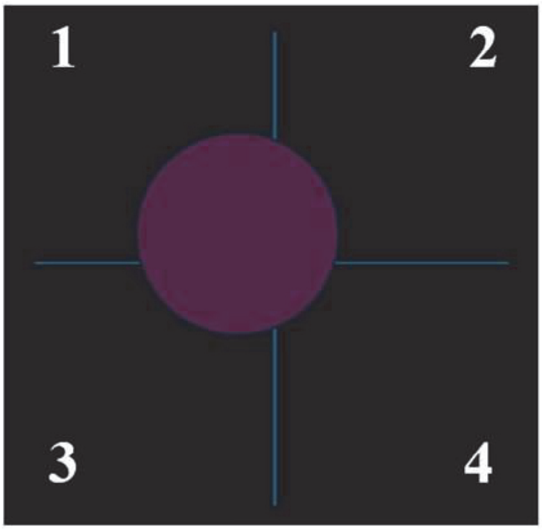

Figure 1.6. Basic quadrant photodetector structure.

Figure 1.6. shows the general structure used in QPDs. The regions numbered 1-4 are independent photodiodes that generate photocurrent response to the incident light, their outputs are converted to voltage response by transimpedance amplifier circuits. Using the channel voltages, the position of the incident beam with respect to the origin is calculated by the equation (1.9) and (1.10).

$$x = k.\sigma_x = k.\frac{(V_2 + V_4) - (V_1 + V_3)}{V_1 + V_2 + V_3 + V_4} \quad (1.9)$$

$$y = k.\sigma_y = k.\frac{(V_1 + V_2) - (V_3 + V_4)}{V_1 + V_2 + V_3 + V_4} \quad (1.10)$$

The terms σ_X and σ_Y are the normalized voltage output signals, term “k” is the coefficient factor that is determined by the shape and size of the spot used in the measurements.[24]

To determine this factor, spot position measurement experiments are conducted. Du et. al used 266 nm pulsed laser system to evaluate positioning performance, firstly an area of 600 x 600 µm is scanned with a step size of 100 µm the readouts are used in (1.9) and (1.10) to calculate σ_X and σ_Y terms.[25] Parameter k is often found by linear fitting of the data obtained by the measurements to actual mechanical positions of the spot.[25,26]

Conventional QPDs are typically silicon based, for instance, Lee and Chen developed a two-dimensional tracking system using silicon (Si) based QPD[27], Wang et al. created a setup that detects positions and deflection angles of the laser beam working in 1550 nm.[28] Noh devised a calibration method to improve measurement accuracy in such systems[29]. Si-based QPDs work in visible and near-infrared regions and suffer in terms of performance due to the background noise introduced by ambient light sources.[30]

To solve this problem 4H-SiC stands as a better alternative material, it absorbs light in near UV region to middle UV and most importantly has low background noise from visible and infrared sources.[31] Qualities of 4H-SiC include high electrical conductivity, thermal stability along with high breakdown voltage and low dark current.[32,33] Additionally, they are capable of functioning under high-frequency, high-power and high-radiation conditions, which makes them ideal for use in extreme environment.[33]

CHAPTER 2

EXPERIMENTAL PROCESSES

2.1. Graphene Synthesis Using Chemical Vapor Deposition Technique

The synthesis of bilayer graphene was performed by chemical vapor deposition method (CVD) due to its high electrical conductivity, optical transmittance and mechanical stability. It is a versatile process for depositing atoms and molecules onto a surface. In atmospheric conditions or under vacuum it has been a prominent method for thin film production[34] Carbon based materials like nanotubes and graphene have been synthesized efficiently using this method.[35] Using CVD, graphene production is achieved at temperatures ranging between 800-1000 °C on transition metals such as nickel (Ni), iridium (Ir) and copper[36] (Cu), gasses such as Methane (CH_4) are used as a carbon source.[37] Large-area and high-quality graphene synthesis can be achieved potentially for industrial applications.[38]

At the start of the process copper foils (99.8% pure, 25 µm thick, Alfa Aeasar) are prepared to be used as a substrate. They are cut into 7.5 x 7.5 mm squares as in Figure 2.1 a) and then cleaned with acetone, IPA and DI for 5 minutes afterwards dried by nitrogen gas.

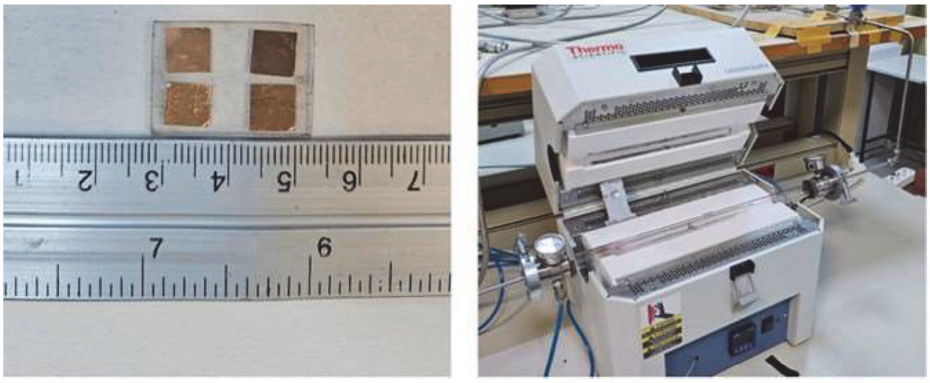

Figure 2.1. Prepared copper foils that are cut 7.5 x 7.5 mm and TF55035C Furnace CVD System

Figure 2.1 shows the TF55035C Split Mini Tube Furnace equipped with 2-inch diameter quartz tube that serves as the reaction environment for the heating, annealing and growth stages. Methane (CH_4), hydrogen (H_2), and argon (Ar) gases are connected to the furnace system and are regulated by MKS Mass-Flo Controllers and MF-1 Flow Meters. These devices are connected to the MKS Multi-Gas Controller 647C which interfaces with a computer to control the gas flow rates depending on the step of process.

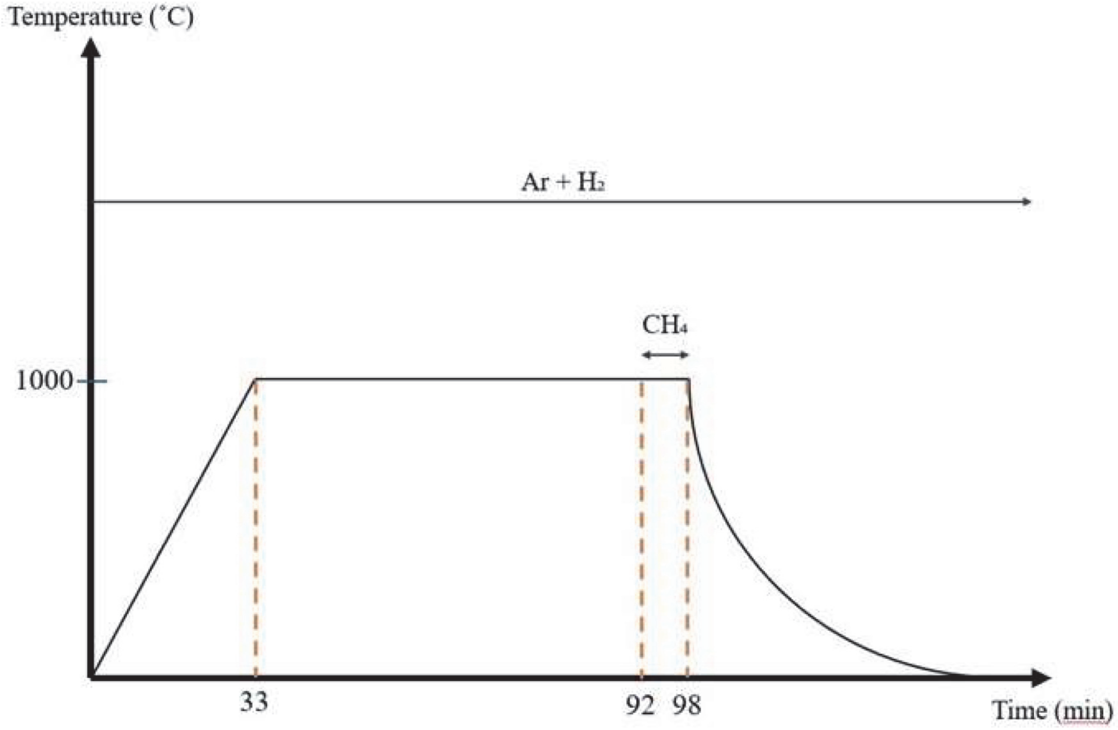

Figure 2.2. Heating profile for bilayer graphene.

As seen in Figure 2.2 the furnace is ramped up to 1000 ˚C in 33 minutes in the meantime to reduce the native oxide layer on copper foils and to form (111) oriented grain boundaries H_2 (20 sccm) and Ar (1000 sccm) are introduced and maintained throughout the entire growth process and cooling included. After annealing is finished CH_4 (10 sccm) flows at the 92-minute mark for 6 minutes and results in the growth of bilayer graphene.

After 98 minutes the heating is stopped and samples are enabled to be cooled rapidly by ambient conditions, at 120 ˚C the samples are taken out of the oven and Microposit S1318 photoresist is drop casted onto the samples covering graphene. Finally, they are annealed at 70 ˚C with Nüve Dry Heat Sterilizer FN 032 furnace for 12 hours, they are then stored in a desiccator environment under vacuum until the transfer process.

2.2. Raman Spectroscopy Measurements

Raman spectroscopy is a non-destructive optical method used to investigate molecular vibrations, crystal structure and electronic properties of materials. A monochromatic laser is directed onto the sample. By this interaction most of the photons that are scattered retain the same energy level as the incident beam named Rayleigh scattering in the literature. Small number of photons interact with the chemical bonds and get effected by the vibrational, rotational or electronic energy as a result the scattered photons have shifted energy. The intensity of the scattered light is detected and plotted as a function of Raman shift (in cm^{-1}).

For graphene research and characterization Raman spectroscopy stands as a reliable and widely used method in various studies the spectrum of graphene has prominent features at D peak (~1350 cm^{-1}), the G peak (~1580 cm^{-1}), and the 2D peak (~2700 cm^{-1}).[39,40] In a Raman spectrum D peak intensity is correlated with disorders while G peak is related with in-plane vibrations of sp_2 bonded carbon pairs and finally 2D peak gives information about the number of layers.[41]

The ratio between the intensities of the peaks gives valuable information about graphene's qualities. I_g/I_{2D} ratio determines the number of layers. The relevant values are ~0.5, ~1 for monolayer and bilayer graphene respectively, in the case of few layers and more the ratio would exceed the value of 1. I_d/I_g serves to quantify the number of defects.

In this study Raman spectroscopy measurement was conducted at Materials Research Centre (MCR) of Izmir Institute of Technology using Renishaw in Via Qontor Raman Microscope shown in Figure 2.3.

Figure 2.3. Renishaw in Via Qontor Raman Microscope at Iztech MCR.

2.3. Thermal Evaporator System

In this work, the device contacts are composed of hold (Au), silicone oxide (SiO_2) and chromium (Cr). Quadrant feature is formed by nickel (Ni). Figure 2.4 shows the thermal evaporation system in QDL which is used to deposit these layers.

Figure 2.4. Nanovak NVTH-350 Thermal Evaporation System is shown on the left. Right image shows inside of the chamber.

In the evaporation chamber there are four crucibles: (1) Cr-plated tungsten wire, (2) SiO_2, (3) Ni and (4) Au. The samples are mounted on a motorized stage (5), which enables uniform condensation of the evaporated material across the substrate surface.

The deposition thickness is monitored in real-time using dual quartz crystal microbalance (QCM) sensors located on both sides of the stage. During the process, evaporation is driven by a direct current power supply, and the rate is controlled by gradually increasing the current. Once the material reaches its evaporation point, the motorized stage is manually activated to ensure uniform film formation.

Before the evaporation process, the samples are cleaned by sonicating in Acetone, IPA and deionized water respectively for 15 minutes. Native oxide layers formed on the SiC substrates are cleaned off by 3% HF solution. The samples were loaded onto the holder and mounted on the thermal evaporation system. The coating processes are conducted at ~$4x10^{-7}$ mbar – at the limit of the turbo molecular pumps capacity to ensure clean environment for evaporation process.

The C-face of the samples are firstly coated with 5/80 nm thickness of Cr/Au to manufacture GND contact of the samples, Cr-plated tungsten wire is outgassed at low power to remove oxidation, the thin layer of Cr provides adhesion between sample surface and Au.

Si-face is coated with 500 nm of SiO_2 material to provide an insulation layer between the metal contact and sample surface. The materials were available in pellet form that contains cavities, to outgas (add specifics duration later) SiO material was subjected to current incrementally for 17 hours. Vacuum was stabilized at ~10^{-7} mbar before reaching the evaporation point. After the SiO was evaporated the process carries on with depositing 5/80 nm of Cr/Au and metal contact production is finished.

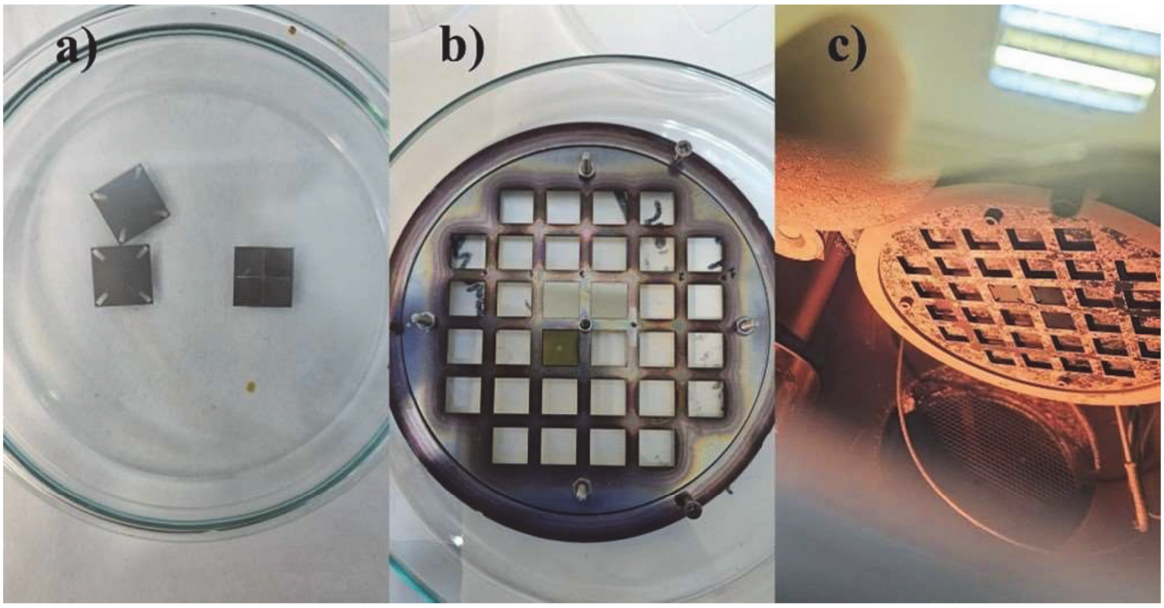

Figure 2.5. (a) Masks used to create the pins and quadrant form on the SiC substrate. B) Sample holder and loaded SiC substrates. C) In-chamber view of the samples during the evaporation process.

After wet transfer is completed, using the mask in Figure 2.5 a) 50 nm Ni was evaporated onto the sample surface creating the cross shape on bilayer graphene which later was oxidized to create an electrical and optical insulator.

2.4. Transfer of Graphene onto the SiC Substrate

After graphene synthesis stage a wet transfer method was employed to transfer p-type bilayer graphene onto the target substrates which were prepared after thermal evaporation of metal contacts, below Figure 2.6. shows the optical microscope image of fully prepared sample, that has BLG transferred and NiO formed.

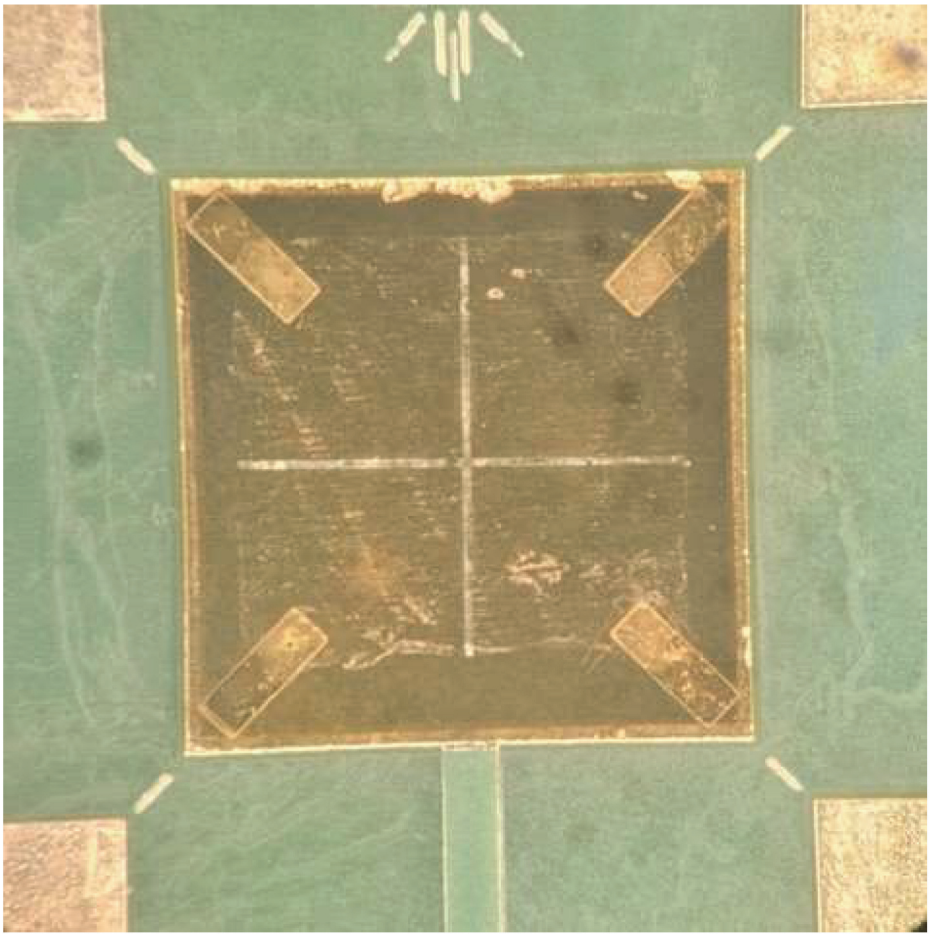

Figure 2.6. Fully prepared QPD device with electrical contacts, BLG transferred and NiO formed, substrate is connected to the PCB by silver paste.

In the first stage of the transfer process given in Figure 2.6, the copper layer of the pre-prepared Cu/Gr/PR samples were etched in a 0.2 M $FeCl_3$ solution for 9 hours. After the etching process, to remove the residual $FeCl_3$ and copper on the graphene surface, the samples were first rinsed in deionized water for 5 minutes and then immersed for 30 minutes in a 3:1 mixture of HCl and deionized water. To eliminate HCl residue the samples were rinsed again in deionized water for 5 minutes.

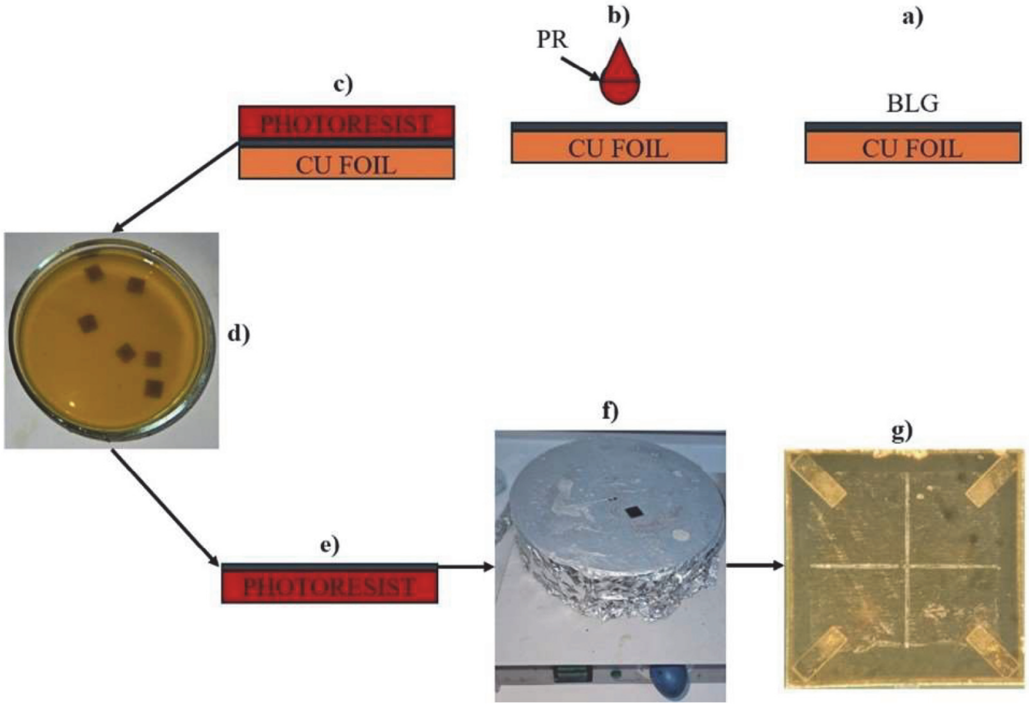

Figure 2.7. Steps of the transfer process illustrated.

Finally to bind the prepared PR/Gr structure onto the SiC substrates the samples are placed on the Au contacts and centered then placed onto the hotplate and then heated at 110 ˚C to promote adhesion to active layer of the substrate. In the final step the PR layer is removed by sequentially immersing in acetone, IPA and deionized water for 5 minutes respectively. As a result of these processes only the bilayer graphene remained on the substrate. The success of the transfer process was confirmed by measuring the resistance between Au contacts.

2.5. Forming Quadrant Structure

To create the quadrant structure the BLG region had to be separated into 4 equivalent regions by an optical isolator in the UV region and also the method needed to create electrical isolation. To achieve this NiO was selected due to its availability and properties. A thin film of 50 nm was thermally evaporated onto a clear quartz wafer, subsequently using TF55035C Split Mini Tube Furnace the Ni sample was heated to 500 ˚C by 10 ˚C/min ramping rate then kept stable for 5 hours. Fresh flow of air was facilitated by directing an AC fan towards the end of the Quartz tube.

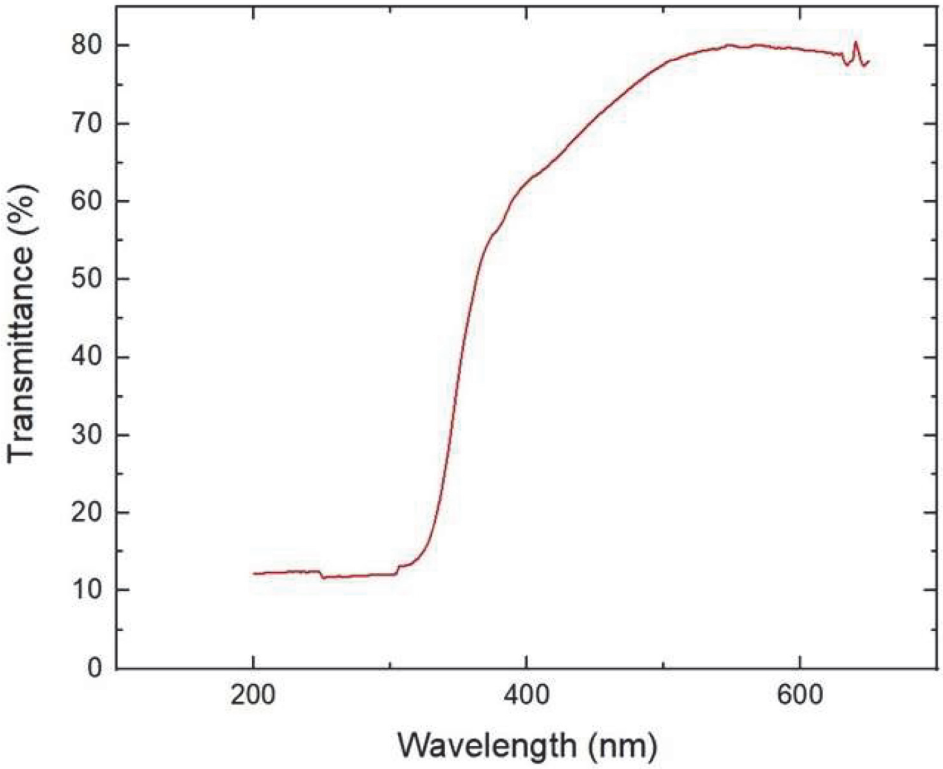

Figure 2.8. Transmittance spectra of NiO thin film.

At Integrated Research Center of Iztech, transmittance measurement of the NiO sample was conducted. The results are shown in Figure 2.8 it shows that NiO is a suitable candidate as an optical isolator to be worked within 250 – 350 nm range. Finally, the same procedure was reapplied to BLG transferred onto clear quartz, using the cross shaped mask at Figure 2.5 a) 50 nm of Ni was evaporated and was later oxidized by the same recipe. The NiO region electrically worked as an insulator and sheet resistance was measured as overload.

After verification finally the same procedure was applied to QPD samples and BLG contact was successfully separated into 4 isolated regions.

2.6. Device Characterization Equipment

To evaluate the electrical performance of the fabricated QPDs, current – voltage (I - V) measurements were performed under dark conditions, device parameters such as dark current, rectification behavior, shunt/series resistance and threshold voltage are obtained this way. Figure 2.9. shows the experimental setup used for these measurements.

In Figure 2.9. a) the optoelectronic and electronic characterization equipment are shown, TTi SMU4001 Source Measure Unit was used for determining the dark behavior of the QPDs. To measure response speed a 280 nm LED driven with Thorlabs DC2200 High-Power LED Controller in PFM mode was used to excite QPDs and responses were monitored by Rigol MSO8204 Digital Oscilloscope.

Figure 2.9 b) shows MBT616D/M 3-Axis Stage with sample holder PCB mounted where positional calibration and spot scanning measurements were realized with 10 µm resolution in x, y, and z directions. Finally in Figure 2.9 c) Thorlabs SLS204 Stabilized Deuterium Light Source is shown. Spectral responsivity measurements were taken in 250 – 350 nm range using UV bandpass filters and QPDs' spectral responsivity values were specified in UV region.

Figure 2.9. a) The Electronic characterization rack containing a TTi SMU4001 Source Measure Unit, a Rigol MSO8204 Digital Oscilloscope and a Thorlabs DC2200 High-POWER LED Controller. B) MBT616D/M 3-Axis Microblock Compact Flexure Stage. c) SLS204 Stabilized Deuterium Light Source (200 – 700 nm).

CHAPTER 3

RESULTS AND DISCUSSION

3.1. Raman Characterization

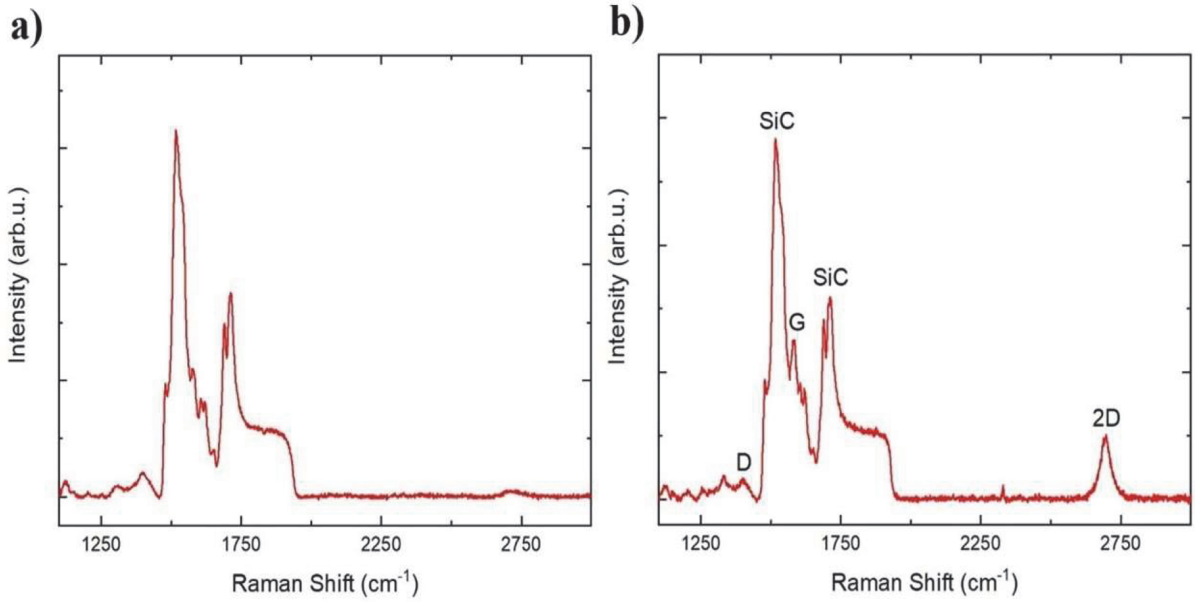

Figure 3.1. a) Raman spectrum of bare Si-face of 4H-SiC, b) after BLG transfer.

Raman spectroscopy was used to verify the presence and quality of the CVD graphene transferred onto the 4H-SiC substrate. Using the Renishaw inVia Qontor Raman Microscope Raman spectrum was taken for bare 4H-SiC's Si face and on one substrate with bilayer graphene (BLG) transferred, Figure 3.1. a) and b) shows these spectra, at b) it is seen that the spectrum exhibits characteristic graphene features which includes a G peak located around 1575 cm^{-1} and a 2D peak near 2690 cm^{-1}. In this work a well-established method to produce bilayer graphene was employed, in recent studies using the same recipe as in[18] bilayer graphene was produced. It is clear in the Raman spectra (Figure 3.1. b)) that high quality bilayer graphene was produced in the process given the D peak and the consistence along with the prominence of the G and 2D peaks.

3.2. Electronic Characterizations of Gr/SiC Quadrant Photodetector

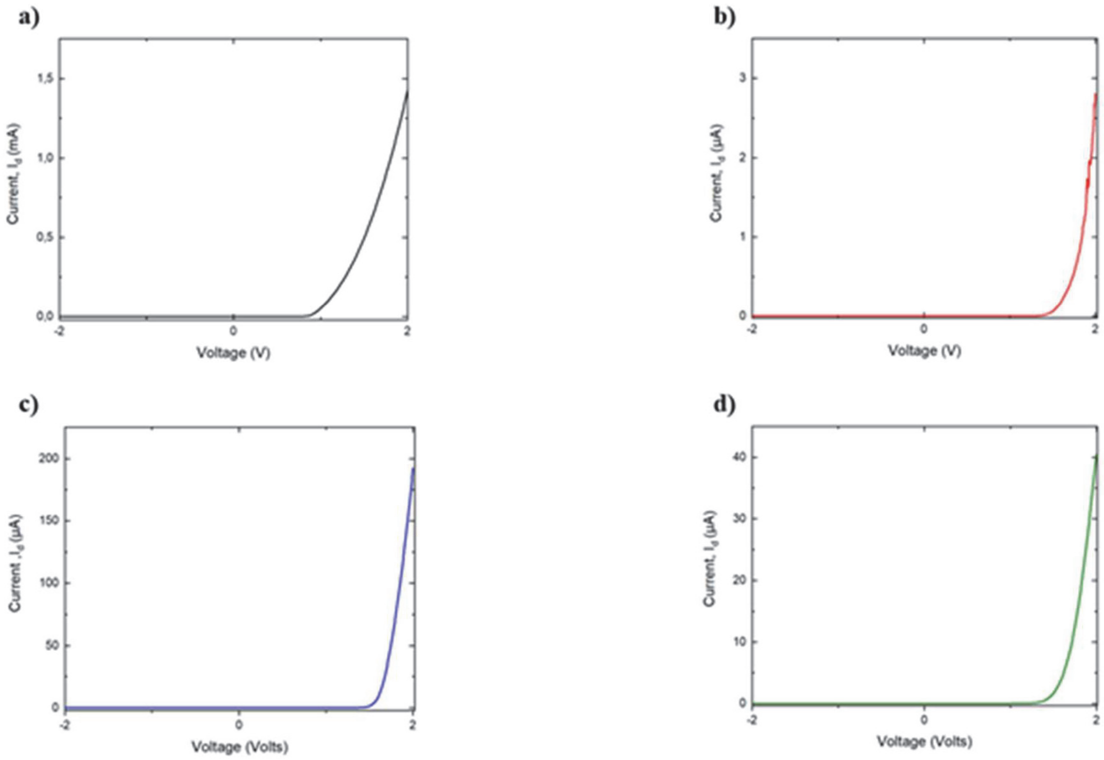

Figure 3.2. I-V measurements in dark environment for a) Channel 1, b) Channel 2, c) Channel 3, d) Channel 4.

The fabricated quadrant photodetector devices consist of four isolated graphene regions transferred onto n-type 4H-SiC (Si-face) substrate. To verify the type of junction formed dark current-voltage (I-V) measurements were conducted on each of the four quadrants in the range of -2V to +2V at stable room temperature environment to evaluate the rectifying behavior and calculate important parameters. Figure 3.2 a)-d) shows the resulting measurements, for comparison.

All four quadrants exhibit nonlinear and asymmetric behavior which is characteristic of Schottky-type rectification. The zero bias dark current has been found as -48.7 pA, -46.8 pA, -48.2 pA and -43.1 pA for quadrants 1 - 4 indicative of minimal leakage in the absence of an external field. A semi logarithmic graph is included in Figure

3.3. To compare channel behavior, it is found that channels become forward biased at 0.5225, 0.7588, 0.6426 and 0.6667 V respectively.

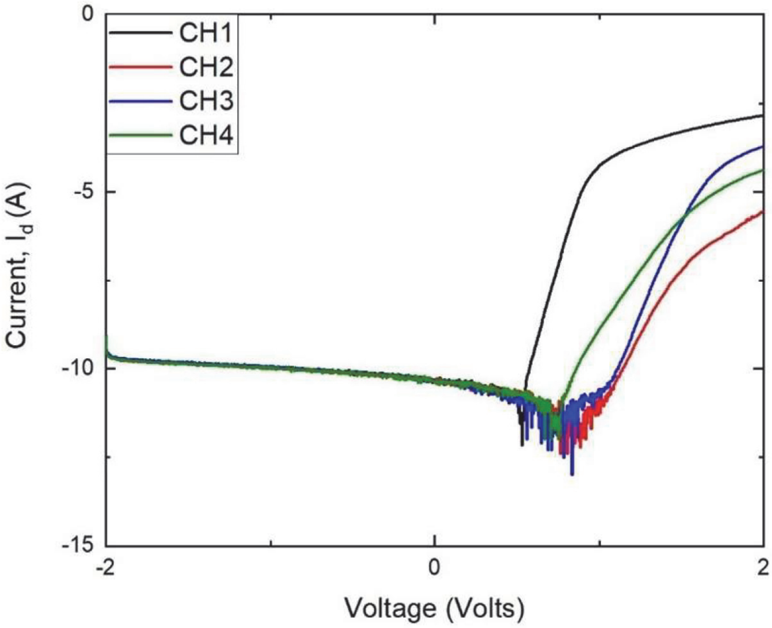

Figure 3.3. Semi-logarithmic scale of I-V curves of each quadrant channel.

For quantitative analysis the electrical performance was analyzed using thermionic emission model (TE) which explains current transport across the Schottky barrier as[15]:

$$I = I_0 \left[exp\left(\frac{qV}{\eta k_B T}\right)\right] - 1 \qquad (3.1)$$

Where I_0 denotes the reverse saturation current and η the ideality factor, q is charge, k is the Boltzmann constant and finally T is the temperature. To extract the diode parameters Cheung's method, which is derived from thermionic emission model, was employed and the method proved useful for predicting the behavior of the quadrant channels for the position mapping experiment.[15]

$$\frac{dV}{dln(I)} = IR_s + \frac{\eta kT}{q} \qquad (3.2)$$

By the slope of equation (3.2) series resistance and ideality factor was obtained, Schottky barrier height was determined by using H(I) function which is shown in equation (3.3).[15]

$$H(I) = V - \frac{\eta k}{q}\ln\left(\frac{I}{AA^{*}T^{2}}\right) = IR_s + \eta\Phi_B \qquad (3.3)$$

In (3.3) $A = 0.1369\ cm^2$ is the junction area of each quadrant and $A^* = 146\ A/cm^2.K^2$ is the Richardson constant for 4H-SiC.[42] All measurements are performed at stable room temperature environment which is T = 300 K. The calculated ideality factor and barrier height values are shown in Table 3.1 below. Hight ideality factors in Channels 1 and 2 suggest that there may be non-uniformity in Gr/SiC contact, local impurities may have occurred in the transfer process.

Table 3.1. Computed ideality factor and Schottky barrier height values of each channel.

Channels	Ideality Factor (η)	Schottky Barrier Height (Φ_B)
Channel 1	11.15	0.727 eV
Channel 2	16.96	0.879 eV
Channel 3	2.99	1.226 eV
Channel 4	4.04	1.117 eV

3.3. Optoelectronic Measurements

3.3.1. Spectral Voltage Responsivity Measurement

Spectral voltage responsivity measurements define a sensors sensitivity towards incident light; it can be defined as the ratio of the photovoltage that is generated in response to the incident UV light. [18]

Due to the limited power of the SLS204 source and the lack of lenses to manipulate the beam size, using a pinhole and optical bandpass filters resulted in sub-nW power. To maintain signal above noise floor, the entirety of the graphene region on the quadrant photodetector was excited using light between 250 – 300 nm of wavelength and 3rd channels' response was measured, to selectively expose the detector to discrete UV wavelengths within this range optical bandpass filters were used. Figure 3.4. shows the results of the measurement. The photodetector shows its highest response at 280 nm wavelength 91.25 V/W.

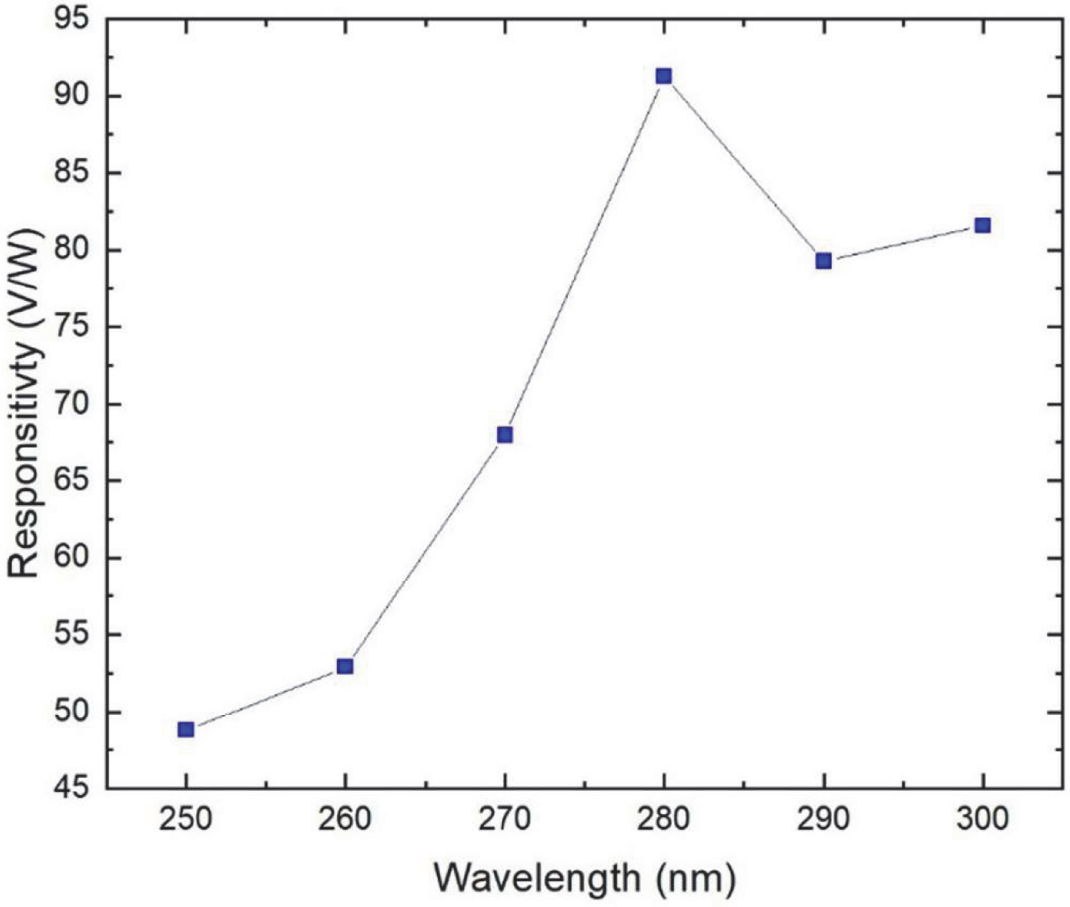

Figure 3.4: Spectral responsivity (R) of Channel 3.

Detectivity (D*) defines the sensors ability to detect weak optical signals from noise.[18] (3.4) shows the mathematical definition:

$$D^* = \frac{\sqrt{A}R(\lambda)}{\sqrt{2qI_d}} \qquad (3.3)$$

The term junction area A is taken as 0.5476 cm^2 which corresponds to area of all quadrants combined. Detectivity plot as a function of wavelength is shown in Figure 3.5.

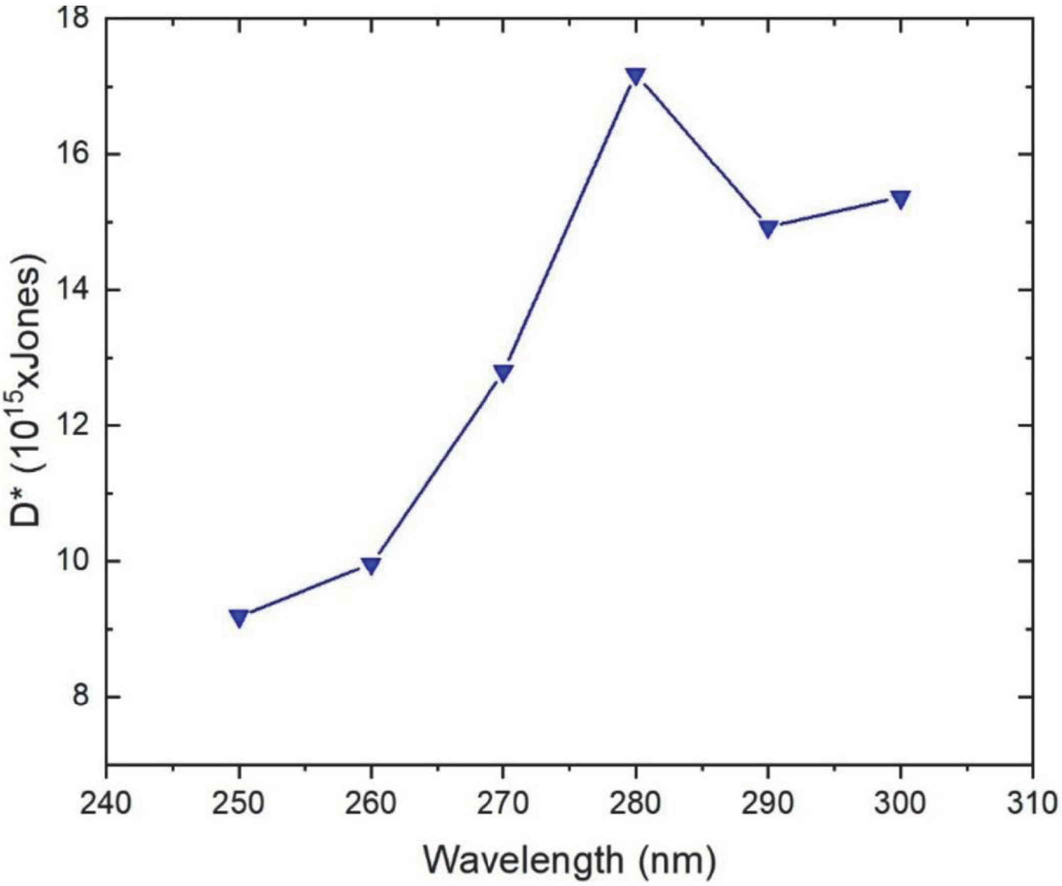

Figure 3.5. Calculated Detectivity.

3.3.2. Time-Dependant Photovoltage Spectroscopy Measurements

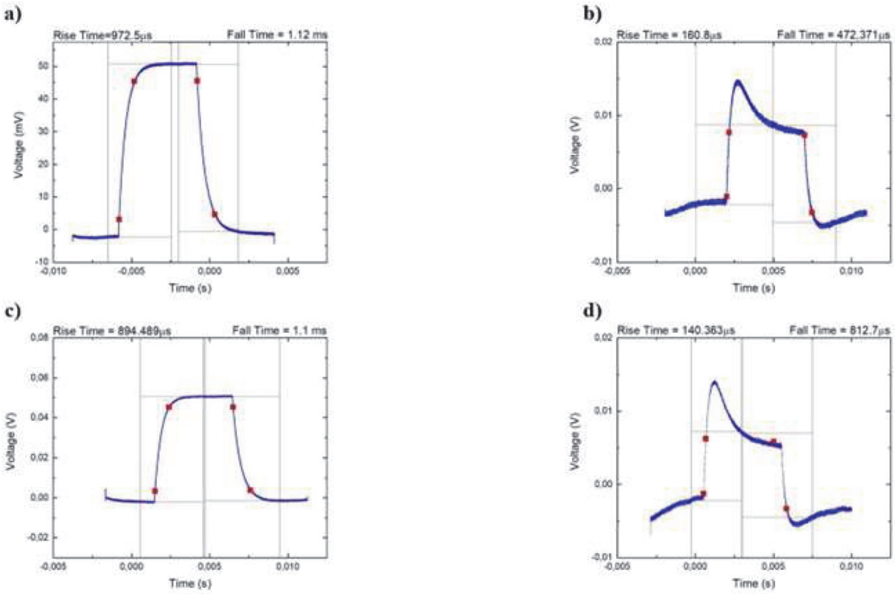

Figure 3.6. Time - dependant photovoltage measurements for the quadrant photodetector channels, a) Channel 1, b) Channel 2 c) Channel 3, d) Channel 4.

Time dependant photovoltage measurements were conducted using Thorlabs DC2200 280 nm LED source. UV light was pulsed at 100 hz frequenzy and sensor response to this input was measured using Rigol MSO0234. Rise time (t_r) and fall time (t_f) was calculated.

Rise time is defined as the time interval in which the measured signal rises from 10% to 90% of its' maximum value, while fall time is the duration it takes for the sensor to return to 10% from 90%, it defines the sensors' ability to catch sudden events occurring in its field of range. In Figure 3.6. a) – d) each quadrant can detect sudden changes of UV light in microseconds range. However, due to graphene impurities or defects imbalances between quadrant response times were observed.

3.3.3. Spot Position Measurement and Sensor Calibration

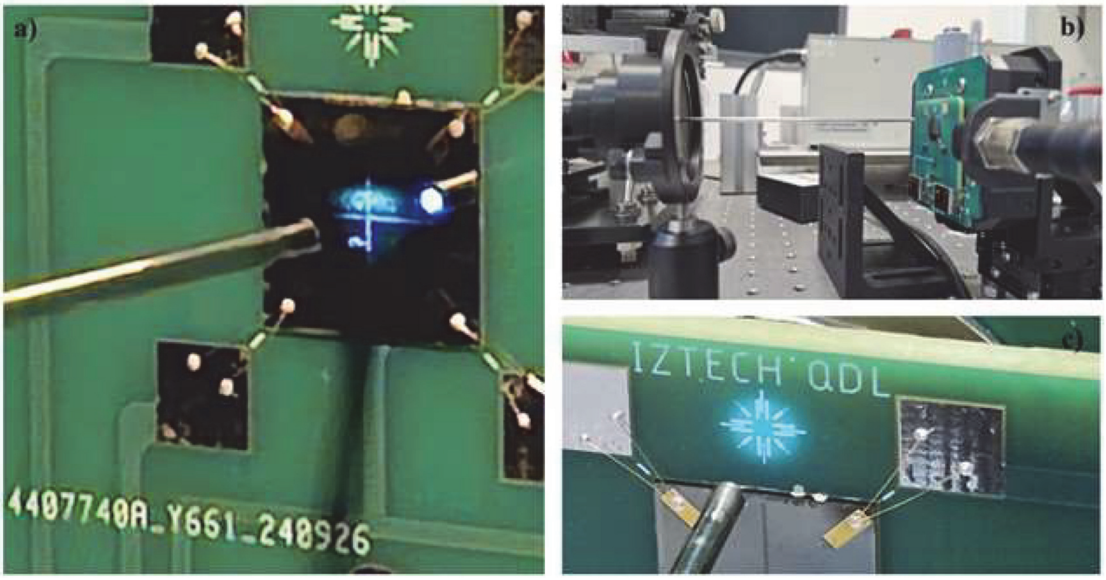

Figure 3.7. a) Centered UV light, b) spot position measurement experiment setup, c) spot centering and spot size calibration.

To assess the positioning performance of the fabricated QPDs, spot position measurement was conducted. Inspired by the methodology outlined in[26], sensor performance was evaluated. In Figure 3.7 b) experimental setup is shown. Thorlabs DC2200 280 nm LED source is set up to illuminate the sample loaded on MBT616D/M 3-Axis Microblock Compact Flexure Stage. Quadrant voltages are measured via calibrated multimeter. Due to the limitations on the experimental setup such as the lack of a collimator and focus lenses, the UV light spot size and position was calibrated by known geometrical references on the printed circuit board, the light spot diameter is 3.4 mm (Figure 3.7. c)).

UV spot was positioned to the central point of the sensor and 1 x 1 mm area was scanned with a step size of 100 µm. To record the measured voltages on the scan points, a graphical user interface program was developed on MATLAB environment, at each point of measurement (x and y) voltage values of each quadrant V1 – V4 are stored. In Figure 3.8. shows the interface that records the voltage responses of the quadrants.

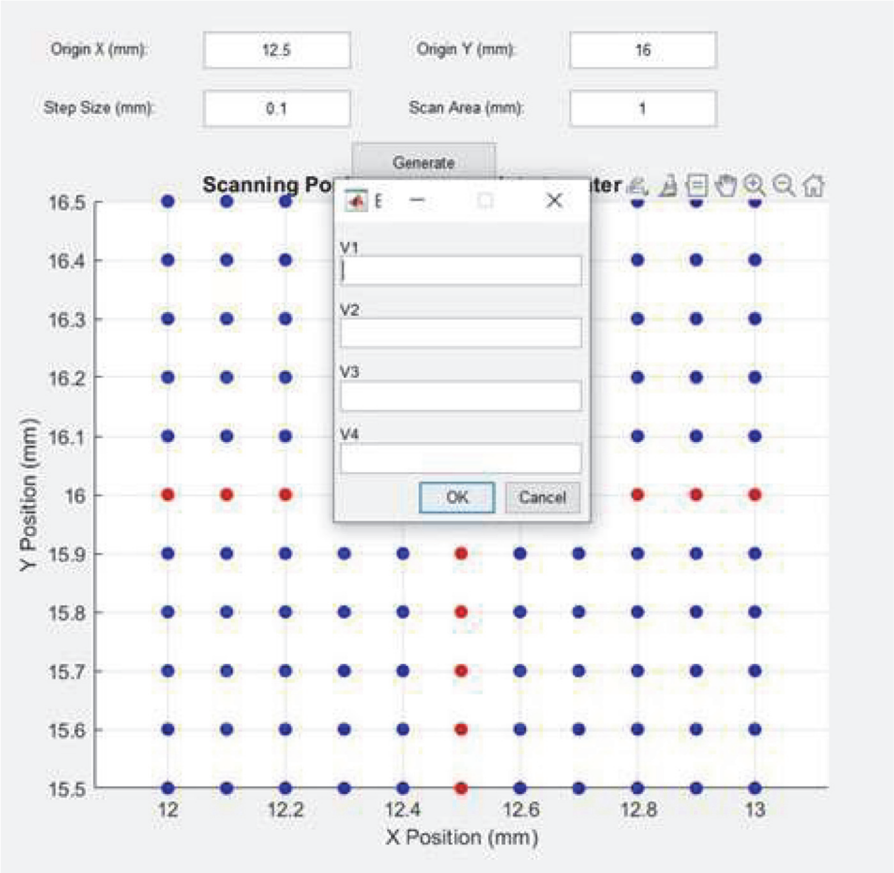

Origin X (mm): 12.5

Origin Y (mm): 16

Step Size (mm): 0.1

Scan Area (mm): 1

Figure 3.8. Graphical user interface program used to create a measurement map and save the quadrant voltages at each position.

After deducing the offset the central point is defined as x = 0 and y = 0. Based on quadrant voltages the position of the spot is determined by (3.4).[26]

$$V_x = \frac{(V_2+V_4)-(V_1+V_3)}{V_1+V_2+V_3+V_4}, \qquad V_y = \frac{(V_2+V_4)-(V_1+V_3)}{V_1+V_2+V_3+V_4} \quad (3.4)$$

The normalized voltages V_X and V_Y are fitted using simple linear regression model against the known mechanical position (3.5). The magnitude of the deviation from the mechanical position is obtained in (3.6).

$$x = a_x V_x + b_x, \qquad y = a_y V_y + b_y \quad (3.5)$$

$$Error = \sqrt{\left(x - x_{fit}\right)^2 + \left(y - y_{fit}\right)^2} \quad (3.6)$$

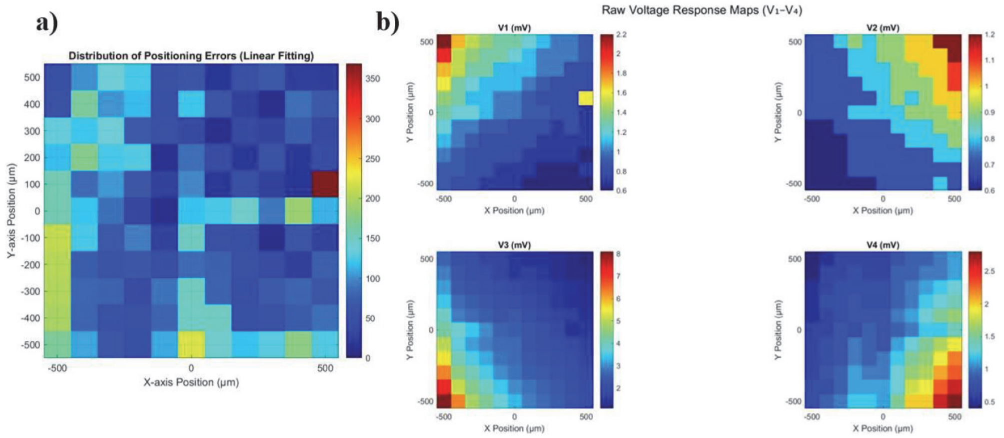

Figure 3.9. a) Positioning error distribution in the scanned area, b) channel voltages 1 – 4 recorded in each scanned position.

Raw voltage values of each quadrant and distribution of mean squared errors are given in Figure 3.9 a) and b). Mean error across all points is found as 86.19 µm and maximum error on a point is 368.81 µm.

CHAPTER 4

CONCLUSION

In this thesis work, we fabricated Gr/4H-SiC based, self-biased, QPD device and investigated using graphene as a p-type electrode in a quadrant photodetector format. Substrates were prepared with thermal evaporation technique, the Schottky Cr/Au contacts on the C-face and SiO/Cr/Au contacts were fabricated in QDL. Bilayer graphene was synthesized using chemical vapor deposition technique and transferred onto n-type SiC substrate. Quadrant structure was formed by Ni evaporation and subsequent oxidization operation done by annealing in atmospheric environment. Raman spectroscopy was employed to verify the existence of bilayer graphene grown on SiC substrate. Having successfully separated the p-type bilayer graphene into 4 electrically isolated regions and proving the graphene electrode, current voltage (I-V) measurements were conducted in reverse and forward bias (-2V – 2V) in a dark environment with stable ambient conditions. Dark current values of the four channels at zero bias were measured as -48.7 pA, -46.8 pA, -48.2 pA and -43.1 pA respectively, Schottky barrier height of each channel were calculated using Cheung's method derived from TE model and barrier heights were found as 0.727 eV, 0.879 eV, 1.226 eV and 1.117 eV for channels 1-4 respectively. Also, ideality (η) factors were found 11.15, 16.96, 2.99 and 4.04. From these results it was deduced that impurities and defects that have occurred during synthesis and transfer process the area of graphene covering the region of channel 1 and 2 has more inhomogeneity which resulted in increased ideality factors and reduced effective barrier heights for channels 1 and 2 in comparison. Highest responsivity was recorded at 280 nm wavelength 91.25 V/W incident light power 81.1 μW consequently detectivity (D*) was calculated and found on the order of ~10^{15} Jones. Spot position measurement was done in a 500 x 500 μm area, scanning with 280 nm UV LED source with 3.4 mm spot size. 121 positions were scanned with 100 μm step size and channel voltages were recorded and processed in custom MATLAB environment. Using coordinate formulas (3.4) normalized voltages were obtained and linear regression model was used (3.5) to fit the calculated positions with real mechanical coordinates. Mean error of 86.19 μm and maximal error of 368.81 were recorded, the results correlate with the findings of dark current-voltage measurement.

In conclusion QPD sensor with Gr/4H-SiC architecture was successfully fabricated and implementing p-type bilayer graphene as an electrode was experimentally validated. In future studies this architecture could be improved by homogenous graphene electrode and advancing the device architecture.

REFERENCES

1. Novoselov, K. S.; Geim, A. K.; Morozov, S. V.; Jiang, D.; Katsnelson, M. I.; Grigorieva, I. V.; Dubonos, S. V.; Firsov, A. A. Two-dimensional gas of massless Dirac fermions in graphene. *Nature* **2005**, *438*, 197–200.

2. Geim, A. K.; Novoselov, K. S., The rise of graphene. Nature Materials **2007**, 6 (3), 183-191.

3. Venables, J. A.; Spiller, G. D. T.; Hanbücken, M. Nucleation and growth of thin films. *Rep. Prog. Phys.* **1984**, *47* (4), 399–459.

4. Evans, J. W.; Thiel, P. A.; Bartelt, M. C. Morphological evolution during epitaxial thin film growth: Formation of 2D islands and 3D mounds. *Surf. Sci. Rep.* **2006**, *61*, 1–128.

5. Novoselov, K. S.; Geim, A. K.; Morozov, S. V.; Jiang, D.; Zhang, Y.; Dubonos, S. V.; Grigorieva, I. V.; Firsov, A. A. Electric field effect in atomically thin carbon films. *Science* **2004**, *306* (5696), 666–669.

6. Dash, G. N.; Pattanaik, S. R.; Behera, S. Graphene for electron devices: The panorama of a decade. *IEEE J. Electron Devices Soc.* **2014**, *2* (5), 77–104.

7. Castro Neto, A. H.; Guinea, F.; Peres, N. M. R.; Novoselov, K. S.; Geim, A. K. The electronic properties of graphene. *Rev. Mod. Phys.* **2009**, *81* (1), 109–162.

8. Giubileo, F.; Di Bartolomeo, A. The role of contact resistance in graphene field-effect devices. *Prog. Surf. Sci.* **2017**, *92*, 143–175.

9. Sarma, S. D.; Adam, S.; Hwang, E.; Rossi, E., Electronic transport in two dimensional graphene. Reviews of Modern Physics **2011**, 83 (2), 407.

10. Sze, S. M.; Ng, K. K. *Physics of Semiconductor Devices*; 3rd ed.; Wiley: Hoboken, NJ, **2007**.

11. Di Bartolomeo, A. Graphene Schottky diodes: An experimental review of the rectifying graphene/semiconductor heterojunction. *Phys. Rep.* **2016**, *606*, 1–58.

12. Tongay, S.; Schumann, T.; Miao, X.; Appleton, B. R.; Hebard, A. F. Tuning Schottky diodes at the many-layer-graphene/semiconductor interface by doping. *Carbon* **2011**, *49*, 2033–2038.

13. Zeghdar, K.; Dehimi, L.; Saadoune, A.; Sengouga, N. Inhomogeneous barrier height effect on the current–voltage characteristics of an Au/n-InP Schottky diode. *J. Semicond.* **2015**, *36* (12), 124002.

14. Roccaforte, F.; La Via, F.; Raineri, V. Ohmic contacts to SiC. *Int. J. High Speed Electron. Syst.* **2005**, *15* (4), 781–820.

15. Cheung, S. K.; Cheung, N. W. Extraction of Schottky diode parameters from forward current–voltage characteristics. *Appl. Phys. Lett.* **1986**, *49* (2),

16. Guo, H.; Liu, B.; Huang, B.; Chen, H. Broad spectrum high responsivity photodetector based on SiC–graphene transistor. In *2017 14th China International Forum on Solid State Lighting: International Forum on Wide Bandgap Semiconductors China (SSLChina: IFWS)*; IEEE: Beijing, China, **2017**; pp 159–162.

17. Li, X.; Zhu, H.; Wang, K.; Cao, A.; Wei, J.; Li, C.; Jia, Y.; Li, Z.; Li, X.; Wu, D. Graphene-on-silicon Schottky junction solar cells. *Adv. Mater.* **2010**, *22*, 2743–2748.

18. Jehad, A. K.; Unverdi, O.; Celebi, C. High voltage response of graphene/4H-SiC UV photodetector with low level detection. *J. Alloys Compd.* **2023**, *969*, 172288.

19. Guziewicz, M.; Grochowski, J.; Borysiewicz, M.; Kaminska, E.; Domagala, J. Z.; Rzodkiewicz, W.; Witkowski, B. S.; Golaszewska, K.; Kruszka, R.; Ekielski, M.; Piotrowska, A. Electrical and optical properties of NiO films deposited by magnetron sputtering. *Opt. Appl.* **2011**, *41* (2), 431–440.

20. Y. Li, K. Zhou, and Z. Zhang, “An improved phase detection method for laser guide systems using position sensitive detectors,” IEEE Sensors Lett., vol. 2, no. 2, pp. 1–4, Jun. **2018**.

21. Das, S.; Saha, A. Laser beam position-dependent PSD-based calibrated self-vibration compensated noncontact vibration measurement system. *IEEE Trans. Instrum. Meas.* **2019**, *68* (9), 3308–3320.

22. I. N’Doye et al., “Reduction of the beam pointing error for improved free-space optical communication link performance,” IFAC J. Syst. Control, vol. 16, Jun. **2021**, Art. no. 100154.

23. Castello, M.; Sheppard, C. J. R.; Diaspro, A.; Vicidomini, G. Image scanning microscopy with a quadrant detector. *Opt. Lett.* **2015**, *40* (22), 5355–5358.

24. Wu, J.; Chen, Y.; Gao, S.; Li, Y.; Wu, Z. Improved measurement accuracy of spot position on an InGaAs quadrant detector. *Appl. Opt.* **2015**, *54* (27), 8049–8054.

25. Du, H.; Li, W.; Wang, Y.; Xu, W.; Zhou, D.; Ren, F.; Chen, D.; Zhang, R.; Zheng, Y.; Lu, H. A pulsed ultraviolet laser positioning system based on 4H-SiC four-quadrant photodetectors. *IEEE Photon. Technol. Lett.* **2024**, *36* (11), 697–700.

26. Yang, P.; Wang, Y.; Xu, W.; Zhou, D.; Ren, F.; Chen, D.; Zhang, R.; Zheng, Y.; Lu, H. Ultraviolet spot position measurement based on 4H-SiC quadrant photodetectors. *Chin. Opt. Lett.* **2024**, *22* (11), 112501.

27. Lee, H.-W.; Chen, C.-L. Applying dual-laser spot positions measurement technology on a two-dimensional tracking measurement system. *Meas. Sci. Technol.* **2009**, *20* (12), 125103.

28. Wang, Z.; Zhang, Z.; Zou, K.; Meng, Y.; Hu, X. Silicon four-quadrant photodetector working at the 1550-nm telecommunication wavelength. *Opt. Lett.* **2022**, *47* (16), 4048–4051.

29. Noh, J.-H. Optimization-based calibration process for position-sensitive detector systems. *IEEE Photon. Technol. Lett.* **2020**, *32* (6), 301–304.

30. Guo, H.; Liu, R.; Deng, Z.; Wu, Q. Performance analysis and testing of four-quadrant position sensitive detector. *Adv. Mater. Res.* **2011**, *317–319*, 1107–1113.

31. Zetterling, C.-M.; Lanni, L.; Ghandi, R.; Malm, B. G.; Östling, M. Future high temperature applications for SiC integrated circuits. *Phys. Status Solidi C* **2012**, *9* (7), 1647–1650.

32. H. Guo, B. Liu, B. Huang, H. Chen, 2017. SiC-graphene heterojunction ultraviolet detector, in: 2017 14th China Int. Forum Solid State Light. Int. Forum Wide Bandgap Semicond. China (SSLChina IFWS), IEEE, **2017**: pp. 236–239.

33. Yan, F.; Xin, X.; Aslam, S.; Zhao, Y.; Franz, D.; Zhao, J. H.; Weiner, M. 4H-SiC UV photo detectors with large area and very high specific detectivity. *IEEE J. Quantum Electron.* **2004**, *40* (9), 1315–1320.

34. Ferrari, A. C.; Bonaccorso, F.; Falko, V.; Novoselov, K. S.; Roche, S.; Bøggild, P.; Borini, S.; Koppens, F.; Palermo, V.; Pugno, N.; et al. Science and technology roadmap for graphene, related two-dimensional crystals, and hybrid systems. *Nanoscale* **2015**, *7*, 4598–4810.

35. Reina, A.; Jia, X.; Ho, J.; Nezich, D.; Son, H.; Bulovic, V.; Dresselhaus, M. S.; Kong, J. Large area, few-layer graphene films on arbitrary substrates by chemical vapor deposition. *Nano Lett.* **2009**, *9* (1), 30–35.

36. Li, X.; Cai, W.; An, J.; Kim, S.; Nah, J.; Yang, D.; Piner, R.; Velamakanni, A.; Jung, I.; Tutuc, E.; Banerjee, S. K.; Colombo, L.; Ruoff, R. S. Large-area synthesis of high-quality and uniform graphene films on copper foils. *Science* **2009**, *324* (5932), 1312–1314.

37. Kim, K. S.; Zhao, Y.; Jang, H.; Lee, S. Y.; Kim, J. M.; Kim, K. S.; Ahn, J.-H.; Kim, P.; Choi, J.-Y.; Hong, B. H. Large-scale pattern growth of graphene films for stretchable transparent electrodes. *Nature* **2009**, *457*, 706–710.

38. Bae, S.; Kim, H.; Lee, Y.; Xu, X.; Park, J.-S.; Zheng, Y.; Balakrishnan, J.; Lei, T.; Kim, H. R.; Song, Y. I.; Kim, Y.-J.; Kim, K. S.; Özyilmaz, B.; Ahn, J.-H.; Hong, B. H.; Iijima, S. Roll-to-roll production of 30-inch graphene films for transparent electrodes. *Nat. Nanotechnol.* **2010**, *5*, 574–578.

39. Ferrari, A. C.; Basko, D. M. Raman spectroscopy as a versatile tool for studying the properties of graphene. *Nat. Nanotechnol.* **2013**, *8* (4), 235–246.

40. Malard, L. M.; Pimenta, M. A.; Dresselhaus, G.; Dresselhaus, M. S. Raman spectroscopy in graphene. *Phys. Rep.* **2009**, *473* (5–6), 51–87.

41. Wang, Y. Y.; Ni, Z. H.; Yu, T.; Shen, Z. X.; Wang, H. M.; Wu, Y. H.; Chen, W.; Wee, A. T. S. Raman studies of monolayer graphene: The substrate effect. *J. Phys. Chem. C* **2008**, *112* (29), 10637–10640.

42. Zeghdar, K.; Bencherif, H.; Dehimi, L.; Pezzimenti, F.; Della Corte, F. G. Simulation and analysis of the forward bias current–voltage–temperature characteristics of W/4H-SiC Schottky barrier diodes for temperature-sensing applications. *Solid State Electron. Lett.* **2020**, *2*, 49–54.